Density, elastic constants, and thermal conductivity of interfacially-polymerized polyamide films for reverse osmosis membranes

Jordan M. Dennison,[†] Xu Xie,[‡] Catherine J. Murphy,[†] David G. Cahill[†,‡]*

[†]Department of Chemistry, University of Illinois at Urbana—Champaign, 600 Mathews Avenue, Urbana, Illinois 61801, United States

[‡]Department of Materials Science and Engineering and Frederick Seitz Materials Research Laboratory, University of Illinois at Urbana—Champaign, 104 S Goodwin Ave, Urbana, Illinois 61801, United States

*Corresponding Author, E-mail: d-cahill@illinois.edu

KEYWORDS

Reverse osmosis membrane, elastic constant, thermal conductivity, thin polymer film, time-domain thermoreflectance, Rutherford backscattering spectrometry, interfacial polymerization

ABSTRACT

The thickness, volumetric mass density, longitudinal elastic constant, and thermal conductivity of fully aromatic polyamide reverse osmosis membrane active layers synthesized by interfacial polymerization were measured using a combination of Rutherford backscattering

spectroscopy, optical ellipsometry, atomic-force microscopy, quartz crystal microbalance measurements of areal mass density, picosecond acoustics, and time-domain thermoreflectance (TDTR). A support-free synthesis approach produces smooth three-dimensionally cross-linked polyamide films from m-phenylenediamine (MPD) and trimesoyl chloride (TMC). Films were synthesized at a fixed molar ratio of 99:1 MPD:TMC with 0.1 – 2 wt% MPC and 0.005 – 0.1 wt% TMC. A novel method to measure the areal mass density of nanoscale polymer films by Rutherford backscattering spectrometry was developed to aid in characterization of the volumetric mass density of the membranes. The volumetric mass density and longitudinal elastic constant of free-standing polyamide films increase monotonically as the concentration of monomers used to synthesize the films increases. The small thermal conductance of the interfaces prevents direct measurement of the thermal conductivity of the free-standing films; however, based on the assumption of constant interface conductance and thermal conductivity, the thermal conductivity is ~0.30 ± 0.06 W m^{-1} K^{-1}.

INTRODUCTION

Reverse osmosis is used on an industrial scale to produce fresh water from sea water and brackish water.[1] Thin film composite (TFC) polyamide membranes for reverse osmosis consist of a ~100 nm thick polyamide active layer formed by interfacial polymerization on the surface of a ~50 μm thick polysulfone support membrane. The polysulfone support is formed on a ~100 μm thick polyester backing fabric that provides structural support. The polyamide active layer is a semipermeable barrier that allows passage of water molecules and suppresses the passage of ions.

The density of the active layer is a fundamental property that is closely tied to membrane performance. The mechanism of molecular transport through a reverse-osmosis membrane is

typically attributed to a solution-diffusion process where the permeate dissolves into the polymer and diffuses through spaces between the polymer chains.[2-3] Therefore, the volumetric mass density of the polymer plays an important role in determining molecular transport.[4-6] Recent reports show that the volumetric mass density of free-standing polyamide films is influenced by reaction times and monomer concentrations; typically, as the density of polyamide films increases, water uptake and water flux decline.[7-8]

Characterization of a TFC active layer is challenging because the active layer is thin and the signal from many analytical techniques is dominated by the support.[9] The polyamide layer can be isolated by peeling the polyester backing away from the polysulfone support and dissolving the polysulfone layer by repeated rinses with dimethylformamide (DMF).[10-11] The pronounced roughness of polyamide active layers formed on porous polysulfone supports, however, creates challenges for quantitative analysis by many analytical techniques; exposure of the active layer to DMF solvent also changes the properties of the material to a degree that is not fully understood.[12-13] As a result, several groups developed free-standing polyamide membrane materials to better isolate the properties of interfacially-polymerized polyamide while avoiding the uncertainties created by the processing steps needed to separate a polyamide active layer from its polysulfone support. Free-standing polyamide thin films can be synthesized on a sacrificial layer, by electrospray deposition, and by a support-free approach at the interface between two bulk solutions.[7, 12, 14-18] These free-standing films can then be transferred to a porous support to create a TFC membrane, or to a non-porous substrate to facilitate microanalysis.

However, volumetric mass densities (ratio of the areal mass density and the thickness) as high as 2 g cm^{-3} have been reported for free-standing polyamide films.[7] In our view, a mass density of 2 g cm^{-3} is unphysically large for polyamide. As we discuss below, the volumetric mass density

of a commercially-available linear meta-linked fully aromatic glassy polyamide polymer, Nomex, is 1.2 ± 0.1 g cm^{-3} and the largest volumetric mass density we have observed in our interfacially-polymerized layers is 1.26 ± 0.2 g $cm^{-3.}$ Here, we characterize the volumetric mass density of free-standing polyamide films using two independent techniques for the areal mass density (quartz crystal microbalance and a novel Rutherford backscattering spectrometry approach) and two independent techniques for the thickness (atomic force microscopy and ellipsometry).

The elastic constants of materials depend on the strengths and number density of atomic and molecular bonds and therefore provide additional insights on the microstructure. Membranes are operated at high pressures during reverse osmosis which makes the elastic constants an important property to understand.[1] Plastic deformation of the support membrane in the TFC structure has been studied in detail.[19-21] However, there are few reports of the mechanical properties of the polyamide active layer due to the measurement challenges associated with isolating and characterizing the rough nanoscale layer.[7, 12, 22-23] We determine the longitudinal elastic constant C_{11} of free-standing polyamide films using the longitudinal sound velocity v_l as a probe. To our knowledge this is the first use of picosecond acoustics to characterize interfacially-polymerized membrane active layers.

Using the same data that we collect to determine C_{11} we are also able to measure the thermal conductance G of the support-free polyamide films. The thermal conductivity Λ_{PA} of polyamide membrane active layers has not been reported before. While the thermal conductivity is not practically important for understanding membrane performance, it is a fundamental material property that is related to the elastic constants and porosity.[24-25] While it is not the goal of this work to examine porosity directly, porosity is linked to volumetric mass density, thermal transport, and also to the mass transport properties of the membrane materials.[26-27] Here we use TDTR to measure

the thermal conductance of free-standing polyamide films prepared at different monomer concentrations. If we assume a constant value for the interfacial thermal conductance, we can determine the thermal conductivity of interfacially-polymerized polyamide. The thermal conductivity that we measure is consistent with our volumetric mass density and C_{11} measurements.

Synthesis of free-standing polyamide films produces smooth, nanoscale membrane materials that are amenable to characterization by optical techniques. We combine measurements by quartz crystal microbalance, Rutherford backscattering spectrometry, atomic force microscopy, ellipsometry, picosecond acoustics and time domain thermoreflectance (TDTR) to examine the effects of monomer concentration on the volumetric mass density, elastic constant, and thermal transport properties of polyamide membrane active layers.

EXPERIMENTAL SECTION

Materials

M-phenylenediamine (MPD) flakes (99%), 1,3,5-benzenetricarbonyl trichloride (TMC, 98%), calcium chloride (93%), lithium chloride (99%), sodium chloride (99%), and N,N-dimethylformamide (DMF, 99.5%) were purchased from Sigma. Methanol (99.8%) and hexane (99.9%) were purchased from Fisher Chemical. M-Invnomex felt was donated by Mundo Tex Ltd. Poly(methyl methacrylate) (950 K A7 in anisol) was purchased from MicroChem. MPD is stored in a refrigerator. TMC is stored in a desiccator. MPD solutions were prepared in 18 MΩ cm water. TMC solutions were prepared in hexane that is stored over molecular sieves.

Substrate surface treatment

A home-built chamber was used to increase the hydrophilicity of substrates including bare Si wafers, Pt-coated Si wafers, and quartz crystal microbalance sensors by exposing the substrates to ozone prior to film transfer. The chamber consists of a glass bell jar with a port that accommodates a UV pencil lamp (Spectroline 11SC-1, 254 nm). Substrates were placed on a stage in the chamber elevated above 10 mL of water which raises the relative humidity in the chamber. The UV-ozone treatment ran for 15 min.

Support-free synthesis of free-standing polyamide films

We adapted the procedure for the synthesis of support-free polyamide films from Park *et al*, and is illustrated in Scheme 1.[14] A glass petri dish with a diameter of 8 cm serves as a reaction vessel. The petri dish was cleaned in a base bath, rinsed with nanopure water, and then dried in an oven. We synthesized the films by adding 20 mL of MPD solution to the dish (0.1 – 2.0 wt% MPD) and allowing the liquid to sit for a few seconds until the surface is still. We then added 15 mL of TMC solution (0.005 – 0.1 wt% TMC) via Pasteur pipettes by placing the tip of the pipette into contact with the edge of the dish so that the TMC solution spreads on the surface of the aqueous MPD solution. After the final TMC addition, the reaction proceeded for 2 minutes followed by removal of both the aqueous and organic solutions from the dish via Pasteur pipette. Reaction times for similar syntheses reported in the literature range from 1 – 10 min so we selected an intermediate value of 2 min as the reaction time.[7, 14] We rinsed the films by first pipetting ~10 mL of hexane on to the film surface, removing the hexane via pipette, and repeating the process with ~10 mL of water. Film transfer to a silicon wafers and QCM sensors was facilitated by floating the film on ~20 mL of water, sliding the substrate under the film, and lowering the film onto the wafer by removing the water via pipette. Once transferred to a substrate, we stored the films under ambient laboratory conditions in plastic petri dish.

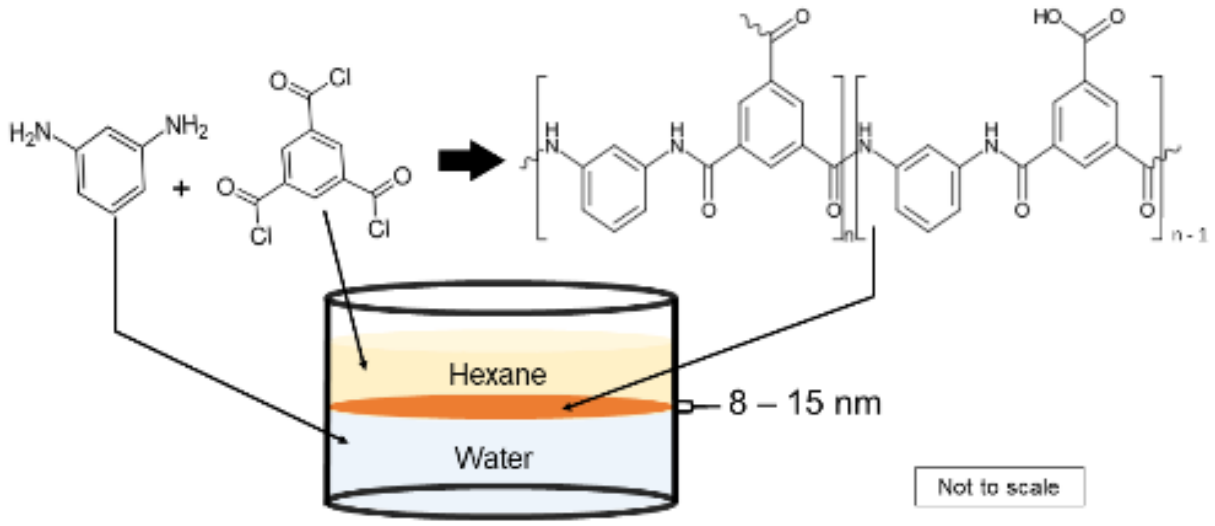

Scheme 1: Synthetic scheme demonstrating the synthesis of free-standing polyamide films.

Preparation of spin-coated polymer films

Nomex is a fully aromatic meta connected linear polyamide (structure shown in Figure S1A). We prepared Nomex solutions by dissolving 2 g of Nomex felt in 50 mL of DMF with 1 g of LiCl and stirring at 90 °C for 3 hours.[28] The Nomex solution was diluted by a factor of two with DMF for spin-coating on UV cleaned Si wafers at 3000 rmp for ~2 minutes. We soaked spin-coated substrates in methanol for three days changing the methanol solution twice per day to dissolve LiCl that might remain in the film. X-ray photoelectron spectroscopy of a ~15 nm Nomex film did not show any chlorine within the detection limit of the instrument.

PMMA control samples were prepared diluting as received solutions of PMMA in ansiol with toluene at a volumetric ratio of either 1:7 or 1:16, and then spin-coating the films at 5000 rmp for ~2 minutes onto Si wafers that were UV treated prior to use. The films were then baked at 50 °C for 5 minutes.

Scanning electron microscopy

Film morphology was imaged using scanning electron microscopy (SEM). Free-standing polyamide films on Si substrates were adhered to Al stubs for imaging. Polymers are electrically

insulating so the samples were prepared for SEM imaging by sputter coating with 5-10 nm of a $Au_{60}Pd_{40}$ alloy to prevent charge accumulation. Images were collected using a JEOL JSM-6060LV SEM at a 30 kV acceleration voltage and 8 mm working distance.

Atomic force microscopy

Atomic force microscopy (AFM) was used to examine film thickness. An Asylum Research MFP-3D AFM was used to collect 50 X 50 µm images. All image analysis was done using the program Gwyddion. Thicknesses were determined using unprocessed AFM images to prevent artifacts in the height data that can result from background subtractions. To measure the thickness of free-standing films, one film at each synthesis condition was scratched with a needle prior to imaging to expose the underlying silicon wafer in three distinct areas at least 0.5 cm apart.[10, 12, 14] The step height of the film was taken to be the thickness (Figure S2). The step height from five different line scans per image from three different images of different areas on the sample were averaged to give the film thickness.

Ellipsometry

Film thickness was measured by spectroscopic ellipsometry on a J.A. Woollam VASE instrument. Spectra were collected from 300-1000 nm at intervals of 10 nm at 50°, 60º, and 70º. Film thickness was determined using the following optical model: Layer 1 = Si (substrate), Layer 2 = SiO_2 (thickness 1.4 ± 0.2 nm), Layer 3 = Cauchy model (*A*, *B*, and thickness = free parameter). The thickness of Layer 3 corresponds to the thickness of the polyamide film.[12] We used a Cauchy model to determine the refractive index *n* of the polyamide layer with respect to wavelength λ in µm: $n(\lambda) = A + (B/\lambda^2)$. Optical parameters, $A = 1.53$ and $B = 0.03$, were initially taken from Karan *et al.*[12] When applied to the optical model, these constants give a thickness value that agrees well with AFM data for samples synthesized at 0.25 wt% MPD and 0.0125 wt% TMC and 0.5 wt%

MPD and 0.025 wt%. These two samples have the same volume mass density (see Figure 3B), 1.1 g cm^{-3}. We used the Lorentz-Lorenz equation to determine *n* for the remaining samples which have different volumetric mass densities ρ: $(n^2 - 1)(n^2 + 2)^{-1} = K\rho$. In this case *K* is a proportionality constant that describes the polarizability of the atoms or molecules that make up the material (m^3 kg^{-1}). The optical constants that we calculated using this approach are tabulated in Table S1, and we assume 8% uncertainty in the refractive index. The thicknesses we report are an average of three different measurements from different areas on at least two different samples.

Rutherford backscattering spectrometry

Areal mass density was determined using Rutherford backscattering spectrometry (RBS). A 2.024 MeV He^+ ion beam with an area of ~2 mm^2 is produced by a National Electrostatics Corporation Pelletron accelerator and directed at the sample at an entrance angle of 22.5°, an exit angle of 55.5°, and backscattering angle of 150°. To improve the accuracy of the measurement, we first transfer the polyamide film onto a ~20 nm thick Pt film on a Si substrate and then coat the polyamide layer with a second 20 nm layer of Pt giving the sample geometry, Pt/polyamide/Pt/Si. We use the width of the Pt peak to determine the areal mass density of the polyamide layer. We chose the 20 nm thickness of Pt because the stopping power of the combined thickness of the Pt layers is comparable to the resolution of the RBS detector (~20 keV). We chose Pt (as opposed to other metals) for this measurement because the large atomic number of Pt provides a large Rutherford cross-section, and Pt resists oxidation. Au would also provide these attributes but Pt is typically more planar than Au, and the use of Pt avoids potential problems caused by the low temperature eutectic reaction of Au and Si.

Spectra were modeled using SIMNRA.[29] The alpha particle fluence (number of particles times the solid angle of the detector) is determined by fitting the height of the silicon edge. The

energy calibration is adjusted to match the Si and Pt edges. The detector energy resolution is determined by fitting the slope of the high energy edge of the Pt peak. The thicknesses of the Pt layers in the model are adjusted so that the integration of Pt counts in the model matches the integration of the Pt counts in the data. The composition of the polyamide layer is held constant at 50.0% C, 8.33% N, 8.33% O, and 33.33% H. The areal mass density of the polyamide layer is adjusted to fit the width of the Pt peak. Areal mass densities reported are from a single measurement on a single sample.

Quartz crystal microbalance

The areal mass density of free-standing films was measured by quartz crystal microbalance (QCM). Chrome/gold 5 MHz sensors and a Model QCM200 from Stanford Research Systems were used. Prior to use, the hydrophilicity of the surface of the QCM sensor was increased by UV-ozone treatment as described above. The frequency of the hydrophilic sensor was recorded. Free-standing polyamide films were floated onto the sensor, and the sensor was dried for 20 min at 105 ºC in an oven. The dry mass of the film was determined by first drying the coated sensor for 2 min at 200 °C on a hot plate, and measuring the frequency in an N_2 atmosphere. Reported areal mass densities are the average of three replicate samples. Based on thermogravimetric analysis of polyamide thin film composite membranes reported in the literature, we do not expect the heating steps to degrade the free-standing polymer films.[30]

Water sorption was determined by QCM by establishing the dry mass as described above, and then transferring the dry sample to a sandwich size Ziplock bag with a small beaker containing 5 mL of either pure water, saturated NaCl, saturated $CaCl_2$, or saturated LiCl solutions corresponding to 100%, 75%, 40 %, and 15% relative humidity respectively.[31] Samples were left to incubate for 24 hours, and then the frequency was recorded in the humid environment.

Time-domain thermoreflectance (TDTR) and picosecond acoustics

Samples were coated with ~90 nm of Al by magnetron sputtering. Because this procedure involves pumping the sputter chamber to ~5 x 10^{-8} mTorr, the materials analyzed by TDTR and picosecond acoustics are assumed to be free of adsorbed water. We assume that exposure to high vacuum and sputter coating does not change the volumetric mass density of the polymer.[24, 32]

Ultra-fast lasers are needed to capture the time scales of acoustic wave propagation (nm ps^{-1}), and heat diffusion (~100 nm^2 ns^{-1}) in nanoscale materials. The TDTR system uses a mode-locked Ti:sapphire laser tuned to 783 nm and a repetition rate of 80 MHz. A polarizing beam splitter divides the laser output into pump and probe beams. The power of the pump beam is set to 8 mW and the probe beam power is set to 4 mW. The intensity of the pump beam is modulated with an electro-optic modulator at 10.1 MHz synchronized with an RF-lock-in amplifier. A time delay is imposed on the arrival of the pump and probe beams at the surface of the sample by a mechanical delay stage in the path of the probe beam. The pump and probe beams are overlapped on the sample which has been coated with an Al thin film transducer and focused using a 5× objective lens giving a laser spot size of ~10.7 μm. A photodiode is used to detect the reflected probe beam while light from the pump beam is blocked from reaching the detector by spatial filtering and two-tint wavelength filtering.[33] The signal is measured by a lock-in amplifier connected to the photodiode.

Thermal conductivity was determined by fitting the ratio of the in-phase (V_{in}) and out-of-phase (V_{out}) signal components with a heat diffusion model in which the thermal conductivity of the polymer layer is the only free variable.[34] The heat capacity per unit volume of polyamide is assumed to be 2.0 ± 0.5 x 10^6 J m^{-3} K^{-1} based on the volume specific heat capacity of Kevlar (the structure of Kevlar is shown in S1B), and estimate the error in heat capacity based on the range of

heat capacity values that are typical for amorphous polymers.[32] The speed of sound was determined by analyzing picosecond acoustic signals at short delay times from 0 – 80 ps. All thicknesses used in TDTR data analysis were determined using AFM. The Matlab code used in this analysis was written by Dr. Gregory T. Hohensee.[35]

RESULTS AND DISCUSSION

Support-free free-standing polyamide films

Free-standing films were made from compositions of the monomer reactants between 0.1–2.0 wt% MPD and 0.005–0.1 wt% TMC. Figure 1 shows SEM micrographs of the top surface (hexane side) of free-standing polyamide films as monomer concentration is increased. Conventional TFC membranes formed by interfacial polymerization on porous polysulfone supports are rough due to leafy protrusions that create a ridge and valley structure uniformly covering the surface.[36] In contrast, the free-standing films in Figure 1 are relatively smooth with sparse compact features. At the lowest concentrations of monomer reactants, the surface of the free-standing film is nearly featureless; protrusions become more prevalent as the monomer concentrations increase. The protrusions on the free-standing film are compact nodules and appear to have a structure that is distinct from the folded and leafy features of TFC membranes.[37] RMS roughness values are reported in Table S2. At monomer concentrations below 2.0 wt% MPD and 0.1 wt% TMC, the RMS roughness is much less than the thickness of the film, and above this concentration the roughness and thickness approach similar values. The film morphologies shown in Figure 1 agree well with the work of Park *et al*. and Jiang *et al*.[7, 14]

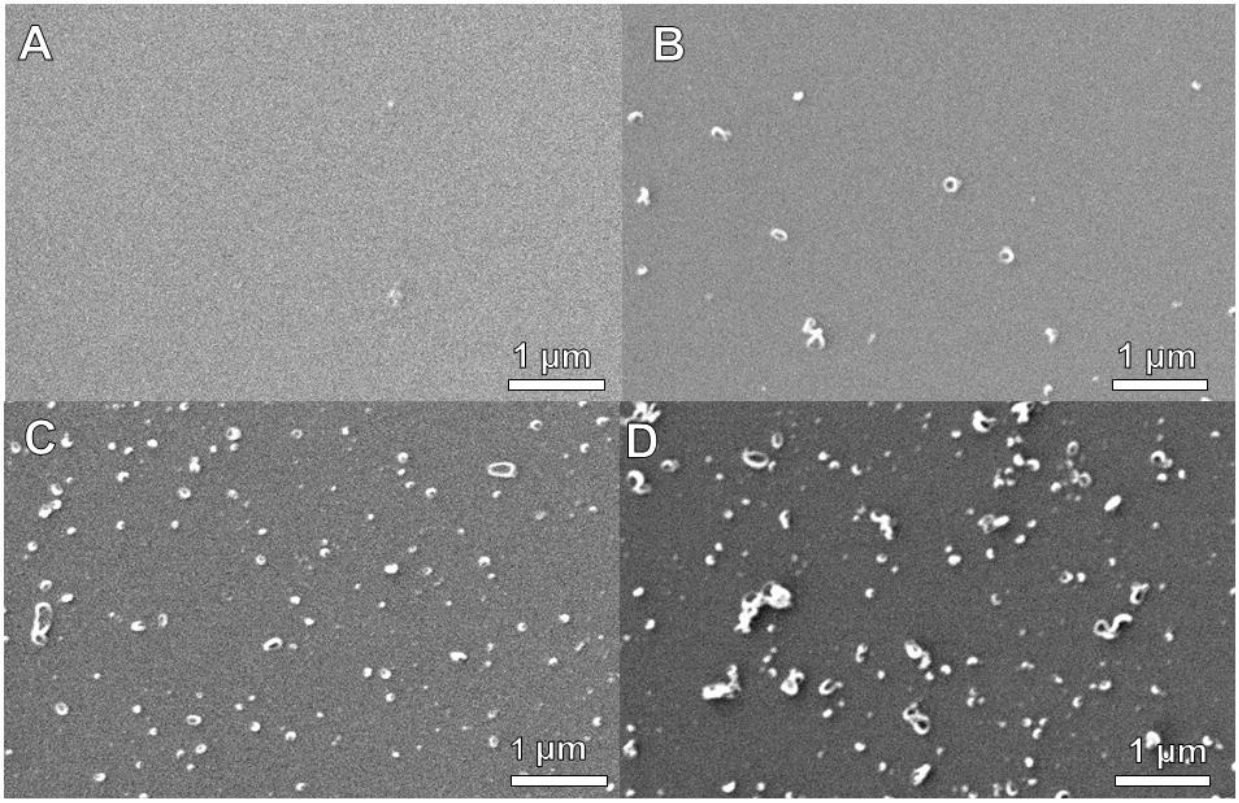

Figure 1. SEM micrographs of the top (hexane facing) surface of free-standing polyamide films prepared using A) 0.1 wt% MPD and 0.005 wt% TMC, B) 0.5 wt% MPD and 0.025 wt% TMC, C) 1.0 wt% MPD and 0.05 wt% TMC, and D) 2.0 wt% MPD and 0.1 wt% TMC.

We do not yet understand why support-free films are typically smoother with more compact features than films synthesized with the same monomer concentrations on porous polysulfone supports. Some control over the morphology of TFC active layers can be exercised using chemical additives, co-solvents, and surfactants,[38-41] but in fact, the mechanistic origins of the leafy structures on TFC membranes are unknown. Ghosh and Hoek posit that the loose leafy TFC structures are caused by the aqueous solution flowing out of the pore structure of the support and spreading laterally on the surface.[38] Khorshidi *et al* note that the concentration dependence of membrane morphology suggests that the diffusion rate of MPD into the organic phase dictates the formation of leafy structures.[42-43] Li *et al*. theorize that the interface with the polysulfone support

is made turbulent by Marangoni convection as the liquid emerges from the pores.[44] Karan *et al*. hypothesize that convection occurs because of heat generated by the formation of polyamide results in Rayleigh-Bénard convection which causes the film to roughen due to instabilities at the hexane interface as a result of poor heat conduction into the support.[8, 12]

However, the evidence is not strong for these hypotheses because the expected Rayleigh number is small due to the small temperature rise from polyamide formation. Constants used in the following calculations are tabulated in Table S3. The enthalpy of the formation of the amide bond between an aromatic acid chloride and an aromatic primary amine is -149 kJ mol^{-1}, and the concentration of amide bonds in a fully aromatic three-dimensionally cross-linked membrane is 11.7 M; therefore, the enthalpy for the formation of 1 cm^2 of film at a thickness of 10 nm (approximately the thickness of free-standing films, see Figure 3A) is -1.74 μJ.[45-46] Given that we expect the thickness of the polyamide film to reach ~10 nm in ~1 s,[47] the power per area P produced by the interfacial polymerization of 1 cm^2 of polyamide is ~1.7 mW cm^{-2}. The total temperature rise for this reaction system over 1 s is given by $\Delta T = P(t)^{1/2}\left(\left(\Lambda_{H_2O}C_{vH_2O}\right)^{1/2} + \left(\Lambda_{Hexane}C_{vHexane}\right)^{1/2}\right)^{-1}$ where Λ is thermal conductivity in W m^{-1} K^{-1} and C_v is the volume-specific heat capacity in J m^3 K^{-1}. This give a total 0.01 K temperature rise from the formation of 1 cm^2 of film. On a localized level, if we estimate that the area of one protrusion on the membrane surface is ~100 nm x 100 nm, temperature rise from radial heat flow away from the protrusion is given by $\Delta T = PA\Lambda_{total}^{-1}z^{-1}$ where A is a 10,000 nm^2 area, Λ_{total} is the sum of the thermal conductivity of the water soaked polysulfone support membrane $\Lambda_{PS+water}$ and the hexane Λ_{hexane}, and z is the dimension of a polyamide protrusion (100 nm). We estimate $\Lambda_{PS+water}$ by assuming that the surface porosity of a polysulfone ultra filtration membrane is ~5% ; therefore, $\Lambda_{PS+water} = (0.95)\Lambda_{PS} + (0.05)\Lambda_{water}$ = (0.95)(0.2 W m^{-1} K^{-1}) + (0.05)(0.6 W m^{-1} K^{-1}) =

0.22 W m^{-1} K^{-1}.[48] Given that Λ_{hexane} is 0.15 W m^{-1} K^{-1}, Λ_{total} is 0.37 W m^{-1}. This gives a temperature increase of ~5 μK. While this is a simplified picture, the magnitudes of the temperature change are small over the relevant length scales. The Rayleigh number R_L expected for a 5 μK temperature perturbation in hexane is given by

$$R = \frac{g\beta}{v\alpha}\Delta T L^3 = 0.04 \quad (1)$$

Where g is the acceleration due to gravity (9.8 m s^{-2}), β is the thermal expansion coefficient of hexane in (1.4 x 10^{-3} K^{-1}), α is the thermal diffusivity of hexane (1 x 10^{-7} m^2 s^{-1}), v is the kinematic viscosity of hexane (4.5 x 10^{-7} m^2 s^{-1}), [49] and L is the thickness of the hexane reservoir in m (in this case 0.003 m based on the volume of hexane and the dimensions of the evaporation dish). This value is small and does not support the hypothesis that heat from the reaction drives instability through buoyancy changes in hexane at the interface.[36]

We measured both the areal mass density and the thickness of the free-standing films by two independent approaches. RBS is an ion beam analytical technique that measures the energy of backscattered high energy He ions. Helium ions lose energy in the sample due to two processes: electronic stopping, and Rutherford scattering. Interactions with electrons in the sample reduce the energy of ions without causing significant changes to the trajectory. The amount of energy lost to this electronic stopping mechanism is dependent on the areal mass density of the material.[50] Rutherford scattering is Coulomb scattering between the nuclear charge of the alpha particle and the nuclear charge of the target atoms. The energy spectrum of backscattered He^+ contains information about the identity, quantity, and depth of the atoms comprising the sample.

Free-standing polyamide films are too thin to be analyzed directly by Rutherford scattering from the C, N, and O atoms in the film. However, the areal mass density can be determined through

the stopping power when the film is sandwiched between two 20 nm Pt films on an Si substrate. The polyamide layer increases the total stopping power of the sample causing the Pt peak in the RBS spectrum to broaden and split.

Figure 2A shows the Pt peak in the RBS spectrum of a single 20 nm Pt layer (Pt/Si), and 2B shows the spectrum of a control sample with two separate 20 nm Pt layers deposited on top of each other (Pt/Pt/Si). Modeling the Pt/Pt/Si sample as a single Pt layer does not fully account for the breadth of the peak. This indicates that there is more stopping power in the Pt/Pt/Si sample than a model of pure Pt can account for. Figure 2B shows the same Pt/Pt/Si sample modeled with a layer of carbon added between the two Pt layers (Pt/C/Pt/Si) to improves the fit. In this case, the best fit is obtained using a 1 μg cm^{-2} layer of carbon. (At the atomic mass density of graphite, 1μg cm^{-2} of areal mass density is equivalent to a thickness of 4.5 nm.) Hydrocarbon contamination is plausible because the sample was exposed to "dirty" environments during UV treatment, and during the process of floating the film onto the substrate. Samples were always handled with tweezers while wearing gloves to avoid contamination by oils or salts.

Uncertainties in the determination of the energy resolution, inaccuracies in the tabulated stopping powers, and uncertainty in the degree of cross-linking of the polyamide affect the accuracy of our measurement of the areal mass density of polyamide. Variation in the energy resolution is ~1 keV which contributes ~2% error.[51] Stopping powers used in RBS analysis for polymeric materials typically have ~5% uncertainty.[52-53] Interfacially- polymerized polyamide is not fully cross-linked so in calculating the areal mass density of the material we must estimate the elemental composition.[54-55] Changing the composition of polyamide in the model by 5% (for example decreasing O content by 5% and concurrently increasing N content by 5%) changes resulting areal mass density by 1%. Given that the O and N content of interfacially-polymerized

TFC active layers reported in the literature is between ~10 – 15 % we expect that the uncertainty in the degree of cross-linking adds ~1% error.[54]

To account for the added stopping power from carbon contamination, the polyamide films are transferred on to Pt-coated Si substrate so that half of the surface is covered with the polyamide film and half of the Pt-coated Si substrate is exposed. This geometry provides a built-in control that has been exposed to all the same processing steps as the polyamide sample. An example is demonstrated in Figure 2C which shows the RBS spectrum of a 0.1 wt% MPD and 0.005 wt% TMC sample modeled to include a carbon contamination layer. The areal mass density of the polyamide film is 0.92 μg cm^{-2}.

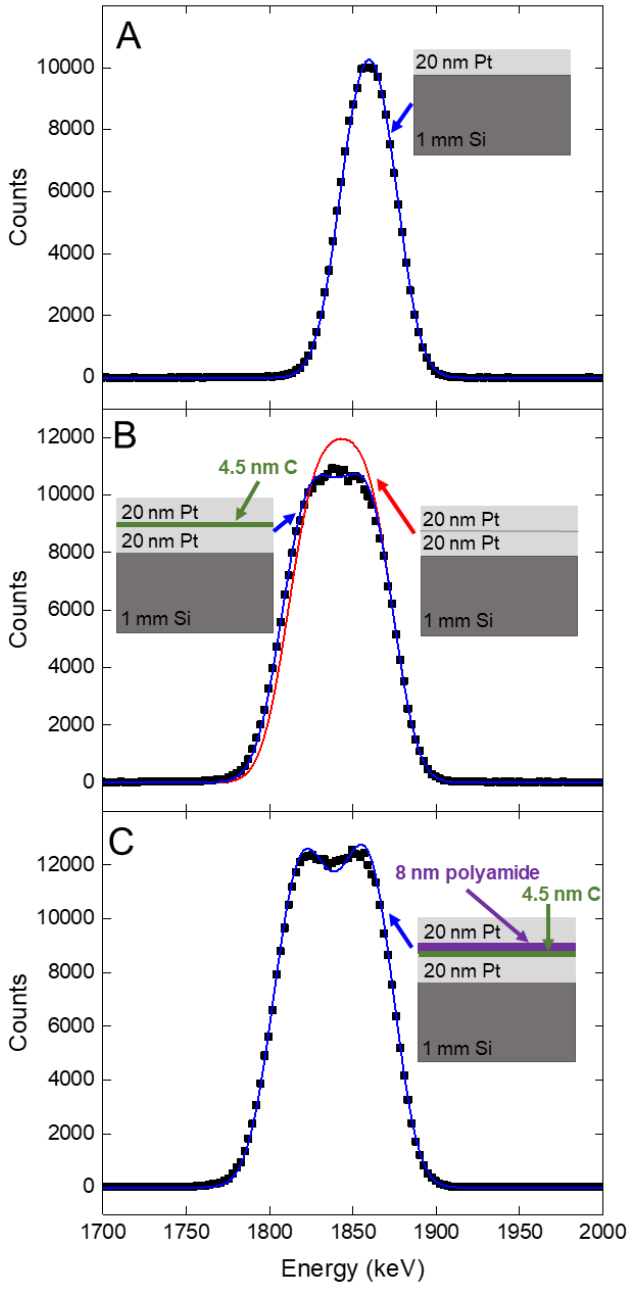

Figure 2. Raw RBS data are shown as black squares, and the modeled data are shown as solid lines. A) An RBS spectrum from a Pt/Si sample. B) An RBS spectrum from a Pt/Pt/Si sample modeled with and without additional stopping power from carbon contamination. The red line represents the fit to the data without carbon contamination, and the blue line represents the fit including carbon contamination. C) An RBS spectrum from a 0.1 wt% MPD and 0.005 wt% TMC

film modeled with an added layer of carbon contamination based on the fit to the Pt/Pt/Si sample shown in B. Insets depict the sample geometry.

Figure 3A shows the areal mass density and thickness of free-standing polyamide films with respect to monomer concentration measured using two independent approaches for each property. We find excellent agreement between RBS and the quartz crystal microbalance (QCM) measurements. QCM frequency shifts as a result of film transfer range from -45 ± 3 to -113 ± 5 Hz as monomer concentration increases. Sample-to-sample mass variability is 5–10 % based on three replicate syntheses, and the long-term stability of the measurement is ± 1 Hz contributing 1–2% uncertainty. We assume that all water sorbed to the polymer is removed by drying, but any residual moisture will affect the accuracy of the QCM measurement. Both measurement approaches show that the areal mass density of the films approximately doubles from 0.9 to 2.0 μg cm^{-2} as monomer concentration increases from 0.1 – 2.0 wt% MPD and 0.005 – 0.1 wt% TMC. The areal mass density of the support-free films is ~10% of the areal mass density of the rougher thicker TFC polyamide active layers which are 20 - 35 μg cm^{-2}.[7, 46, 56]

Thicknesses were determined using ellipsometry and step profiles from AFM images, and again both measurement approaches are in good agreement. AFM step profiles shown in Figure S2 taken from areas ~0.5 cm apart show that the thickness is homogenous across tens of μms at different locations on the film. Film thicknesses increase gradually with monomer concentration showing self-limiting film growth. Thickness increases from 9 ± 1 nm at 0.1 wt% MPD and 0.005 wt% TMC to 15 ± 2 nm as the monomer concentrations increases twentyfold to 2.0 wt% MPD and 0.1 wt% TMC. These values agree with reports of similar support-free systems.[7, 15] We measured thicknesses at ambient humidity of ~35% while areal mass density was measured under dry

conditions. Therefore, we have not accounted for swelling of the polyamide layers which could increase the thickness by 8% to 15% according to neutron reflectivity measurements of free-standing polyamide films.[8] We use thicknesses from AFM in all of the following analyses because *n* must be accurately known for ellipsometry of thin layers; the uncertainty in *n* is ~8% which results in ~7% uncertainty in thickness.

The volumetric mass density of free-standing polyamide films with respect to monomer concentration is shown in Figure 3B. Densities were calculated using the areal mass densities determined by QCM and RBS and thicknesses determined by AFM. The volumetric mass density increases with monomer concentration by ~20% from 1.1 ± 0.2 to 1.3 ± 0.2 g cm^{-3}. In comparison, the volumetric mass density of commercial membrane active layers is 1.24 g cm^{-3}.[10, 46] Previously reported volumetric mass densities of free-standing polyamide films range from 0.6 to 2 g cm^{-3} depending on reaction conditions.[8, 12]

The volumetric mass density of TFC active layers is heterogenous with respect to depth stemming from the heterogenous morphology, but the volumetric mass density of smooth free-standing films is more homogenous.[8, 37, 57] Molecular simulations of support-free interfacial polymerization of polyamide films that are ~ 8 nm thick shows some depth dependence on the volumetric mass density with the inner core of films being more dense than the outer ~2 nm.[6] However, recent neutron reflectivity measurements show that the volumetric mass density of smooth free-standing films is homogenous with respect to depth which is corroborated by cross-sectional SEM images of free-standing polyamide films show that the films are contiguous through the thickness.[7-8] The structure of the compact protrusions that emerge as shown in Figure 1 are not well characterized and could be points of density heterogeneity if they are hollow like the structures that form on TFC active layers.

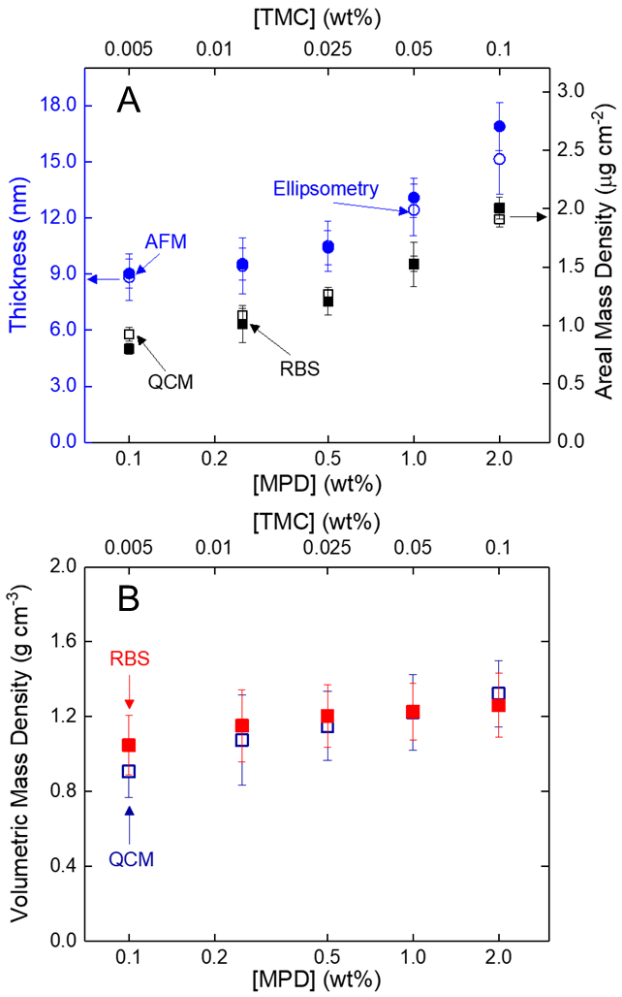

Figure 3. (A) Thickness determined by AFM (open circle) and spectroscopic ellipsometry (filled circle) and areal mass density determined by QCM (open square) and RBS (closed square) of free-standing polyamide films. (B) Volumetric mass density of free-standing polyamide films calculated using the areal mass density of dried films measured by QCM (open square) and RBS (closed square) and thicknesses measured by AFM.

The hydration of membrane active layers is affected by the volumetric mass density amongst other parameters. Sorption of water vapor by free-standing polyamide films as measured by QCM is shown in Figure 4. The mass of sorbed water with respect to relative humidity is shown

in Figure 4A, and the mass change as a percentage of the total mass of the film is shown in Figure 4B. Note that swelling induced by water absorption was not evaluated in this study. Without measuring swelling we cannot differentiate between mass changes due to water absorption into the polymer network and adsorption to the surface so we use the more general term, sorption. The stability of the QCM sensor over time is ± 1 Hz. This is negligible when measuring the mass of the film itself, but the frequency shifts due to water sorption are ~3 – 9 Hz, which is pushing the limits of the measurement. In agreement with previous studies, we find that films with a lower volumetric mass density prepared at low monomer concentrations uptake more water as a percentage of the mass of the film compared to films with a higher volumetric mass density prepared at high monomer concentration.[5, 7-8] Thicker, denser free-standing polyamide films incorporated into TFC membranes also show reduced water permeance compared to less dense films.[7]

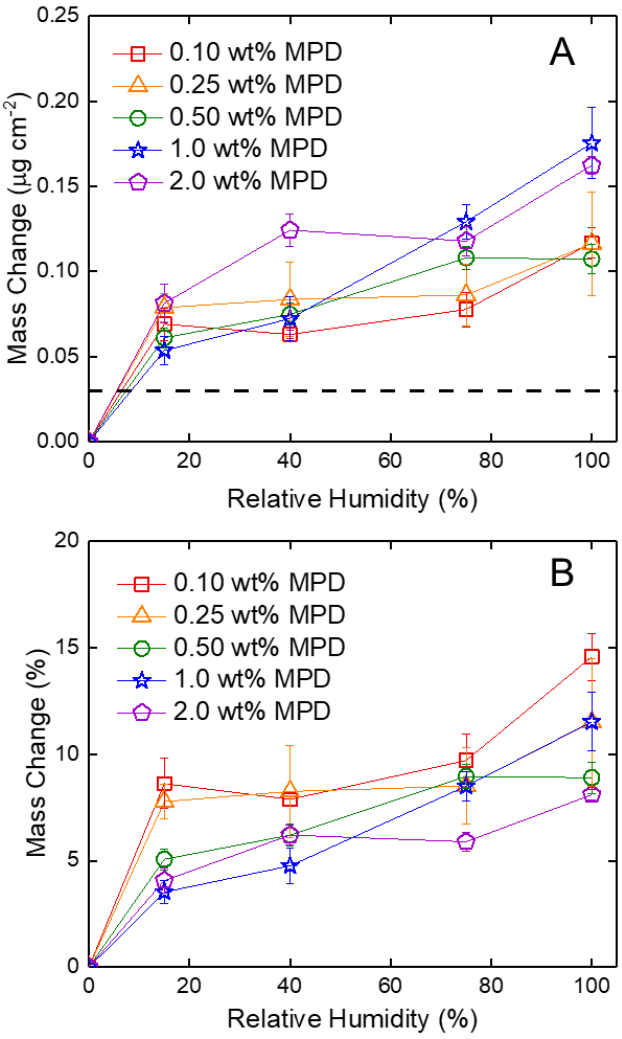

Figure 4. A) Mass change of free-standing polyamide films with respect to relative humidity in µg cm^{-2} of water. The dotted line corresponds to the areal mass of a monolayer of water absorbed to the (0001) face of a quartz crystal for reference. B) Mass change as a percentage of the dry mass of the film. The data points are labeled according to the concentration of MPD used to synthesize the film, and the ratio of MPD:TMC is 20:1.

Elastic constants of free-standing polyamide films

In the following section we first describe how the pump-probe experiment is used to determine the longitudinal sound velocity v_l , present v_l and C_{11} for interfacially-polymerized free-

standing films, and then place our measurements into context with other reports of the mechanical properties of membrane active layers.

We measure the sound velocity of free-standing polyamide films transferred to Si substrates using picosecond acoustics. Heating from the pump beam generates an acoustic wave in response to thermal expansion that propagates through the sample.[58] The acoustic wave is partially transmitted, and partially reflected off interfaces in the sample. The reflected wave causes the reflectance of the Al to change when the wave returns to the surface due to the piezo-optic effect which is detected by the probe beam.

Figure 5A shows representative picosecond acoustics data at short delay times from a 0.1 wt% MPD and 0.005 wt% TMC sample. A small positive peak at 14 ps is attributed to hot electrons in the Al layer, a negative peak at 30 ps corresponds to the echo of the longitudinal wave from the Al/polyamide interface, and a small positive peak at 36 ps corresponds to the echo from the polyamide/silicon interface.[58] Echoes from the Al/polyamide and polyamide/Si interfaces are identified as t_1 and t_2, respectively. The longitudinal speed of sound (v_l) is calculated by

$$v_l = \frac{h}{\left(\frac{t_2 - t_1}{2}\right)} \quad , \qquad (2)$$

where h is the thickness of the polyamide layer measured by AFM (Figure 3A). We validated our approach by measuring the speed of sound in 9.2 ± 1 nm and 23 ± 1 nm spin-coated poly(methyl methacrylate) films (acoustic data for the PMMA controls is shown in Figure S3). The speed of sound in the PMMA films is 3.0 ± 0.3 nm ps^{-1}, in agreement with the reported value.[32]

Longitudinal speed of sound with respect to monomer concentration is presented in Figure 4B and ranges from 2.9 to 3.6 nm ps^{-1}. Over a twentyfold increase in monomer concentration, the speed of sound increases by ~25%. Uncertainty in the speed of sound measurements is ~14% with

~13% contributed by uncertainty in *h* and ~3% contributed by the uncertainty in the echo times. For comparison, the speed of sound in Nomex is 3.1 ± 0.3 nm ps^{-1}.

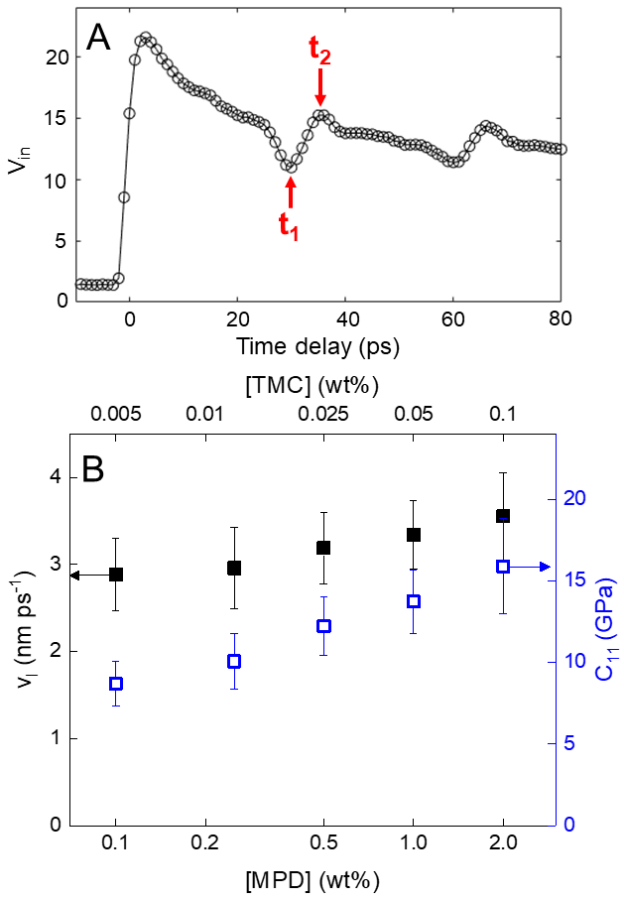

Figure 5. (A) Representative picosecond acoustics (V_{in} from lockin amplifier versus time delay) from a free-standing 0.1 wt% MPD and 0.005 wt% TMC film. (B) v_l (filled square) and C_{11} (open square) of free-standing polyamide films with respect to monomer concentration.

The longitudinal elastic constant (GPa) is related to v_l (m s^{-1}) by volumetric mass density ρ (kg m^{-3}) as $C_{11} = \rho v_l^2$. The fourth-rank elastic constant tensor of an isotropic material has two independent components, typically written using the Voigt notation as C_{11} (the longitudinal modulus) and C_{44} (the shear modulus). In engineering applications, the parameters that describe

the elastic deformation are often written in terms of the Young's modulus E that describes the longitudinal strain of a sample that is subjected to a uniaxial stress and the Poisson ratio v that describes the lateral strain in the same situation. For an isotropic material, C_{11} is related to Young's modulus E and Poisson's ratio v by: $C_{11} = E(1- v)(1+ v)^{-1}(1-2 v)^{-1}$. We have not determined v of our PA layers but $v = 0.35$ is a common value in many polymers.[24] With $v = 0.35$, $C_{11} = \underline{1.6}E$. Our measurement is in the GHz frequency range and therefore is expected to give a larger elastic constant than static measurements.

Figure 5B shows C_{11} with respect to monomer concentration. The longitudinal elastic constant increases from 9 ± 1 to 16 ± 3 GPa over the range of monomer concentrations tested. Amorphous isotropic polymers have longitudinal elastic constants that span a similar range,[32] and the longitudinal elastic constant of Nomex is 11 ± 1 GPa. If we fit the dependence of the elastic constant on volumetric mass density ρ as measured by QCM to a power law, we find C_{11} is proportional to $\rho^{2.3}$ whereas for porous silicas C_{11} is proportional to ρ^{3}.[25]

There are few reports of the mechanical properties of the isolated polyamide active layer. These examples typically decouple the synthesis of the polyamide film from the polysulfone support, mirroring the approach used in this work.[7, 12, 22, 59] Pendant drop tensiometry was used in the early 2000s to examine the rupture strength, and stress-relaxation properties of polyamide films.[22, 55, 59-60] Mechanical stress is applied by injecting liquid into the drop to internally pressurize the system. The rupture strength of the material, is determined by pressurizing the droplet until the film bursts, and is equal to the stress at the instant the film ruptures multiplied by the thickness. Roh *et al*. report increasing rupture strength (~30 – 40 MPa) with increasing monomer concentration.[22] However, these values may not be accurate because film thickness was

determined using TFC membranes prepared at the same reaction conditions as the pendant drop films, but recent work has shown that support-free films are thinner than TFC active layers.[7, 12, 14]

Measurements based on mechanical buckling have been used to determine the Young's modulus of polyamide active layers separated from polysulfone supports, and free-standing polyamide films.[7, 12, 23] A PDMS substrate is stretched lengthwise up to 10% in an elongation holder, and a polyamide film is transferred on top of the PDMS. When the tensile strain applied to the PDMS film is released the PDMS returns to the original length, applying compressive stress to the polyamide film on the surface of the PDMS causing the film to buckle. Chung *et al*. report that the Young's modulus of rough polyamide active layers isolated from the polysulfone supports of TFC membranes is 1.4 ± 0.5 GPa when dry, and 0.36 ± 0.14 GPa when hydrated.[23] The modulus of smooth support-free free-standing polyamide films reported by Jiang *et al*. is larger at 3.6 ± 0.60 GPa. The increased modulus of the free-standing film relative to the conventional material is expected as the free-standing film is smoother that the film isolated from the polysulfone support.

Based on the water sorption data in Figure 4, the films with higher longitudinal elastic constants uptake a less water as a percentage of the total mass of the film. This is noteworthy because films with higher longitudinal elastic constants are more resistant to elastic deformation which is desirable in reverse osmosis applications where large pressures are applied. The strongest films with the highest stiffness exhibit the smallest water sorption which could be an important tradeoff when optimizing membrane performance.

Thermal transport in free-standing polyamide films

In this section we explain how the TDTR measurement works, explain the conditions required to determine Λ_{PA} using TDTR, present our thermal conductance measurements, and interpret the thermal transport data.

TDTR measures the series thermal conductance, G, which includes the thermal conductance of the film and the interfacial thermal conductance across the Al/polymer and polymer/Si interfaces. The pump beam is absorbed by the Al transducer layer causing the temperature at the surface to increase. Heat then flows across the Al/polymer interface into the underlying polymer sample. The probe beam measures temperature changes ΔT through changes in the reflectivity ΔR of the Al layer, $\Delta R = (dR/dT)\Delta T$. For a sample that is thin compared to the thickness of the Al transducer layer, TDTR generally can only determine the effective thermal conductivity of the sample $\Lambda_{eff} = Gh$, where h is the thickness of the sample.[34] In other words, for a thermally-thin sample, TDTR measurements cannot distinguish the thermal conductance of the sample $G_{PA} = \Lambda_{PA}/h$ from the series thermal conductance G_{int} of the two interfaces. Λ_{PA} is the thermal conductivity of polyamide layer.

We determined the thermal conductivity of the polyamide films by modeling the effective thermal conductivity (Λ_{eff}).

$$\Lambda_{eff} = h\left(\frac{h}{\Lambda_{PA}} + \frac{1}{G_{\text{int}}}\right)^{-1} \tag{3}$$

If G_{int} or h are large, Λ_{eff} will not be significantly impacted by G_{int}. However, in our situation, the free-standing polyamide films are thin, and G_{int} is not expected to be large because the film is floated on to the Si support, which may not result in uniform intimate contact between the polymer and the Si. If the thickness of the polyamide layer is comparable to the Kapitza length (K_l), i.e., the thermal conductivity Λ_{PA} divided by the interface thermal conductance G_{int}, then Λ_{eff} is significantly reduced compared to Λ_{PA}. The interfacial thermal conductance of spin-coated polymers is ~100 – 400 MW m^{-2} K^{-1} giving K_l ~1 nm.[32, 61] Given that G_{int} for a spin-coated polymer on Si is expected to be greater than G_{int} for floated films, the Kapitza length of the free-standing

polyamide films will be larger than 1 nm which could be significant considering that the polyamide films are ~9-16 nm thick.

Figure 6A shows G^{-1} plotted as a function of h. The plot is approximately linear. Since the volumetric mass density of the polyamide layer and the thickness increase concurrently, we cannot assume that the thermal conductivity is independent of thickness. Nevertheless, the data can be fit well by an approximately constant thermal conductivity Λ_{PA}=0.3 ± 0.06 W m^{-1} K^{-1} (inverse of the slope of G^{-1} vs h) and an intercept at h=0 of G_{int}=30 ± 6 MW m^{-2} K^{-1}. This value of G_{int} for polyamide films floated onto Si wafers is an order of magnitude smaller than G_{int} of spin-coated polymers and comparable to the conductance we previously observed in studies of transfer-printed metal films.[62] We hypothesize that this is possibly due to the imperfections in the contact made between transfer-printed films and floated films and their respective substrates. The Kapitza length is ~7 nm, comparable to the layer thickness. Because the Kapitza length is large, G_{int} contributes significantly to Λ_{eff} we cannot measure Λ_{PA} for individual interfacially-polymerized layers independent of assumptions about G_{int} nor can we comment on the relationship between membrane performance and thermal transport. However, this value of Λ_{PA} from the slope of Figure 6A is reasonable for a fully dense three-dimensionally cross-linked polymeric material based on the values we report for the volumetric mass density and C_{11}.

Uncertainty in G is calculated by testing the sensitivity of the thermal model to the uncertainty of the fixed parameters in the model including the thickness and heat capacity of polyamide, thickness and heat capacity of the Al, heat capacity of Si, and the laser spot size. Film thickness is the greatest source of uncertainty contributing ~13 % to the model, followed by uncertainty in the Al thickness and the heat capacity of Al each contributing ~5 % and the heat capacity of polyamide contributing <1%. The overall uncertainty in G is ~17 %.

Figure 6B shows an alternative way of plotting the data as Λ_{eff} (equal to Gh) with respect to h^{-1}. We fit Λ_{eff} versus h^{-1} with Equation 3, and use G_{int} and Λ_{PA} as free parameters to determine the best fit. This approach gives G_{int} = 40 ± 7 MW m^{-2} K^{-1} and Λ_{PA} = 0.3 ± 0.06 W m^{-1} K^{-1} which agrees well with the values ascertained by analyzing the linear relationship between G^{-1} versus h (Figure 6A).

The thermal conductivity of a 20 nm ± 2.0 nm thick spin-coated Nomex film is also shown in Figure 6B. Nomex has a volumetric mass density of 1.2 ± 0.1 g cm^{-3} (determined by QCM and AFM). Relative to the three-dimensionally cross-linked free-standing polyamide film, the thermal conductivity of Nomex is smaller.

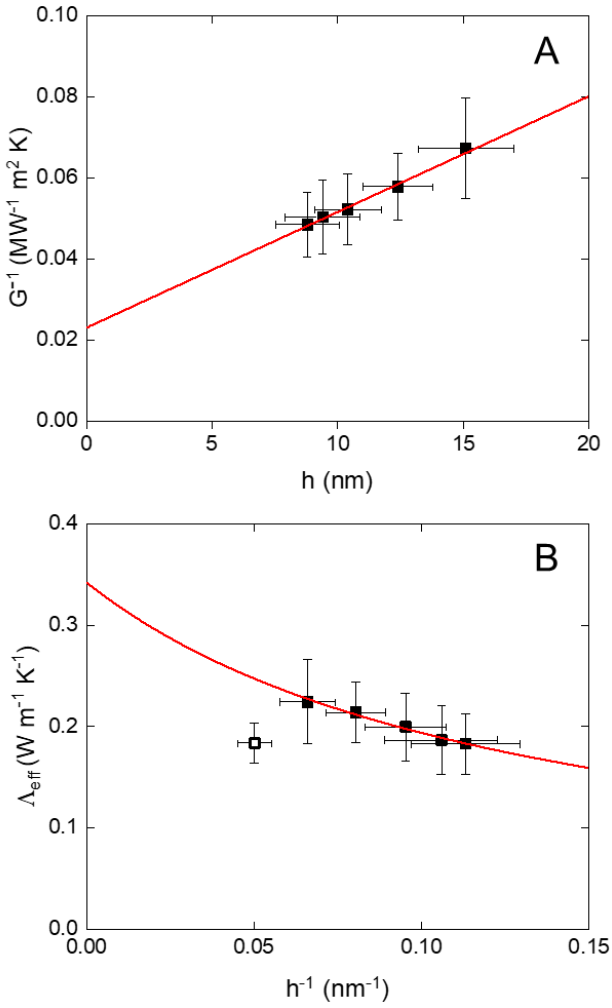

Figure 6. Experimental data are squares and fits to the data are solid lines. Filled squares represent the free-standing polyamide films and the open square is spin-coated Nomex. (A) Inverse thermal conductance (G) of free-standing polyamide films with respect to film thickness (h) fit with a linear regression. The inverse of the y-intercept gives G_{int}=30 ± 6 MW m^{-2} K^{-1} and the inverse of the slope gives Λ_{PA}=0.3 ± 0.06 W m^{-1} K^{-1}. (B) Thermal conductivity (Λ_{eff}) with respect to inverse film thickness (h^{-1}) fit to Equation 3 which gives G_{int} = 40 ± 7 MW m^{-2} K^{-1} and Λ_{PA} = 0.3 ± 0.06 W m^{-1} K^{-1}.

All quantities reported herein are summarized in Table S2.

CONCLUSION

Support-free synthesis of free-standing polyamide films enabled measurement of the volumetric mass density, longitudinal speed of sound, longitudinal elastic constant, and thermal conductance. Notably, this work is one of just a few reports of the elastic constant and the first time that the thermal properties of membrane active layers synthesized by interfacial polymerization have been reported. The volumetric mass density with respect to monomer concentration was measured by independent methods including a novel RBS approach.

The volumetric mass density and elastic constants increase as the monomer concentration increases. The longitudinal speed of sound in the polyamide active layers ranges from 2.9 – 3.6 nm ps^{-1} and increases with monomer concentration concurrent with increasing volumetric mass density. As a result, the longitudinal elastic constant increases from 9 to 16 GPa as the monomer concentrations increase. From a water purification perspective, denser films demonstrate decreased water sorption, but these films are also more rigid and will likely also have higher yield strength.

Plotting thermal conductance with respect to film thickness reveals that the interfacial thermal conductance of the free-standing polyamide films is roughly and order of magnitude lower than that of spin-coated polymers. As a result, the thermal conductance is dominated by the interfaces rather than conductance through the polymer, and we could not examine the relationship between the volumetric mass density and thermal conductivity. However, we estimate $\Lambda_{PA} \approx 0.3$ W m^{-1} K^{-1} based on the assumption that the thermal conductivity does not change significantly with synthesis conditions.

SUPPORTING INFORMATION

Chemical structures of Nomex, Kevlar, and interfacially-polymerized polyamide, AFM step profiles, picosecond acoustics from PMMA, a table of the optical constants used to model ellipsometry data, a table summarizing the measurements performed, and a table detailing the physical properties used in the calculation of the temperature rise from the polymerization

ACKNOWLEDGEMENTS

AFM imaging, SEM imaging, ellipsometry, and TDTR were carried out in the Frederick Seitz Materials Research Laboratory Central Research Facilities, University of Illinois. We thank BP International Center for Advanced Materials for funding this work, and the ICAM 25 team for their helpful insights.

REFERENCES

1. Petersen, R. J. Composite Reverse Osmosis and Nanofiltration Membranes. *J. Membr. Sci.* **1993**, *83*, 81-150.
2. Wijmans, J. G.; Baker, R. W. The Solution-Diffusion Model: A Review. *J. Membr. Sci.* **1995**, *107*, 1-21.

3. Koros, W. J.; Fleming, G. K.; Jordan, S. M.; Kim, T. H.; Hoehn, H. H. Polymeric Membrane Materials for Solution-Diffusion Based Permeation Separations. *Prog. Polym. Sci.* **1988**, *13*, 339-401.
4. Luo, Y.; Harder, E.; Faibish, R. S.; Roux, B. Computer Simulations of Water Flux and Salt Permeability of the Reverse Osmosis Ft-30 Aromatic Polyamide Membrane. *J. Membr. Sci.* **2011**, *384*, 1-9.
5. Kolev, V.; Freger, V. Hydration, Porosity and Water Dynamics in the Polyamide Layer Of reverse Osmosis Membranes: A Molecular Dynamics Study. *Polymer* **2014**, *55*, 1420-1426.
6. Muscatello, J.; Müller, E. A.; Mostofi, A. A.; Sutton, A. P. Multiscale Molecular Simulations of the Formation and Structure of Polyamide Membranes Created by Interfacial Polymerization. *J. Membr. Sci.* **2017**, *527*, 180-190.
7. Jiang, Z.; Karan, S.; Livingston, A. G. Water Transport through Ultrathin Polyamide Nanofilms Used for Reverse Osmosis. *Adv. Mater.* **2018**, *30*, 1705973.
8. Foglia, F.; Karan, S.; Nania, M.; Jiang, Z.; Porter, A. E.; Barker, R.; Livingston, A. G.; Cabral, J. T. Neutron Reflectivity and Performance of Polyamide Nanofilms for Water Desalination. *Adv. Funct. Mater.* **2017**, *27*, 1701738-1701748.
9. Cahill, D. G.; Freger, V.; Kwak, S.-Y. Microscopy and Microanalysis of Reverse-Osmosis and Nanofiltration Membranes. *MRS Bull.* **2011**, *33*, 27-32.
10. Lin, L.; Feng, C.; Lopez, R.; Coronell, O. Identifying Facile and Accurate Methods to Measure the Thickness of the Active Layers of Thin-Film Composite Membranes: A Comparison of Seven Characterization Techniques. *J. Membr. Sci.* **2016**, *498*, 167-179.
11. Freger, V. Swelling and Morphology of the Skin Layer of Polyamide Composite Membranes: An Atomic Force Microscopy Study. *Environ. Sci. Technol.* **2004**, *38*, 3168-3175.
12. Karan, S.; Jiang, Z.; Livingston, A. G. Sub–10 nm Polyamide Nanofilms with Ultrafast Solvent Transport for Molecular Separation. *Science* **2015**, *348*, 1347-1351.
13. Gorgojo, P.; Jimenez-Solomon, M. F.; Livingston, A. G. Polyamide Thin Film Composite Membranes on Cross-Linked Polyimide Supports: Improvement of RO Performance Via Activating Solvent. *Desalination* **2014**, *344*, 181-188.
14. Park, S.-J.; Choi, W.; Nam, S.-E.; Hong, S.; Lee, J. S.; Lee, J.-H. Fabrication of Polyamide Thin Film Composite Reverse Osmosis Membranes Via Support-Free Interfacial Polymerization. *J. Membr. Sci.* **2017**, *526*, 52-59.
15. Park, S.-J.; Ahn, W.-G.; Choi, W.; Park, S.-H.; Lee, J. S.; Jung, H. W.; Lee, J.-H. A Facile and Scalable Fabrication Method for Thin Film Composite Reverse Osmosis Membranes: Dual-Layer Slot Coating. *J. Mater. Chem. A* **2017**, *5*, 6648-6655.
16. Cui, Y.; Liu, X.-Y.; Chung, T.-S. Ultrathin Polyamide Membranes Fabricated from Free-Standing Interfacial Polymerization: Synthesis, Modifications, and Post-Treatment. *Ind. Eng. Chem. Res.* **2017**, *56*, 513-523.
17. Jin, Y.; Su, Z. Effects of Polymerization Conditions on Hydrophilic Groups in Aromatic Polyamide Thin Films. *J. Membr. Sci.* **2009**, *330*, 175-179.
18. Chowdhury, M. R.; Steffes, J.; Huey, B. D.; McCutcheon, J. R. 3D Printed Polyamide Membranes for Desalination. *Science* **2018**, *361*, 682-686.
19. Lee, K. P.; Arnot, T. C.; Mattia, D. A Review of Reverse Osmosis Membrane Materials for Desalination—Development to Date and Future Potential. *J. Membr. Sci.* **2011**, *370*, 1-22.

20. Pendergast, M. T. M.; Nygaard, J. M.; Ghosh, A. K.; Hoek, E. M. V. Using Nanocomposite Materials Technology to Understand and Control Reverse Osmosis Membrane Compaction. *Desalination* **2010**, *261*, 255-263.
21. Chilcott, T. C.; Cen, J.; Kavanagh, J. M. In Situ Characterization of Compaction, Ionic Barrier and Hydrodynamics of Polyamide Reverse Osmosis Membranes Using Electrical Impedance Spectroscopy. *J. Membr. Sci.* **2015**, *477*, 25-40.
22. Roh, I. J.; Kim, J.-J.; Park, S. Y. Mechanical Properties and Reverse Osmosis Performance of Interfacially Polymerized Polyamide Thin Films. *J. Membr. Sci.* **2002**, *197*, 199-210.
23. Chung, J. Y.; Lee, J.-H.; Beers, K. L.; Stafford, C. M. Stiffness, Strength, and Ductility of Nanoscale Thin Films and Membranes: A Combined Wrinkling–Cracking Methodology. *Nano Lett.* **2011**, *11*, 3361-3365.
24. Xie, X.; Yang, K.; Li, D.; Tsai, T.-H.; Shin, J.; Braun, P. V.; Cahill, D. G. High and Low Thermal Conductivity of Amorphous Macromolecules. *Phys. Rev. B* **2017**, *95*, 035406.
25. Costescu, R. M.; Bullen, A. J.; Matamis, G.; O'Hara, K. E.; Cahill, D. G. Thermal Conductivity and Sound Velocities of Hydrogen-Silsesquioxane Low-K Dielectrics. *Phys. Rev. B* **2002**, *65*, 094205.
26. Košutić, K.; Kaštelan-Kunst, L.; Kunst, B. Porosity of Some Commercial Reverse Osmosis and Nanofiltration Polyamide Thin-Film Composite Membranes. *J. Membr. Sci.* **2000**, *168*, 101-108.
27. Yan, H.; Miao, X.; Xu, J.; Pan, G.; Zhang, Y.; Shi, Y.; Guo, M.; Liu, Y. The Porous Structure of the Fully-Aromatic Polyamide Film in Reverse Osmosis Membranes. *J. Membr. Sci.* **2015**, *475*, 504-510.
28. Fridman-Bishop, N.; Freger, V. When Salt-Rejecting Polymers Meet Protons: An Electrochemical Impedance Spectroscopy Investigation. *Langmuir* **2017**.
29. Mayer, M. SIMNRA, a Simulation Program for the Analysis of NRA, RBS and ERDA. *AIP Conf. Proc.* **1999**, *475*, 541-544.
30. Said, M. M.; El-Aassar, A. H. M.; Kotp, Y. H.; Shawky, H. A.; Mottaleb, M. S. A. A. Performance Assessment of Prepared Polyamide Thin Film Composite Membrane for Desalination of Saline Groundwater at Mersa Alam-Ras Banas, Red Sea Coast, Egypt. *Desalination and Water Treatment* **2013**, *51*, 4927-4937.
31. Young, J. F. Humidity Control in the Laboratory Using Salt Solutions—a Review. *J. Appl. Chem.* **1967**, *17*, 241-245.
32. Xie, X.; Li, D.; Tsai, T.-H.; Liu, J.; Braun, P. V.; Cahill, D. G. Thermal Conductivity, Heat Capacity, and Elastic Constants of Water-Soluble Polymers and Polymer Blends. *Macromolecules* **2016**, *49*, 972-978.
33. Kang, K.; Koh, Y. K.; Chiritescu, C.; Zheng, X.; Cahill, D. G. Two-Tint Pump-Probe Measurements Using a Femtosecond Laser Oscillator and Sharp-Edged Optical Filters. *Rev. Sci. Instrum.* **2008**, *79*, 114901.
34. Cahill, D. G. Analysis of Heat Flow in Layered Structures for Time-Domain Thermoreflectance. *Rev. Sci. Instrum.* **2004**, *75*, 5119-5122.
35. Hohensee, G. T. *TDTR_vH3_pub*, https://github.com/gthohensee/TDTR_vH3_pub, 2015.
36. Pacheco, F.; Sougrat, R.; Reinhard, M.; Leckie, J. O.; Pinnau, I. 3D Visualization of the Internal Nanostructure of Polyamide Thin Films in RO Membranes. *J. Membr. Sci.* **2016**, *501*, 33-44.

37. Pacheco, F. A.; Pinnau, I.; Reinhard, M.; Leckie, J. O. Characterization of Isolated Polyamide Thin Films of RO and NF Membranes Using Novel TEM Techniques. *J. Membr. Sci.* **2010**, *358*, 51-59.
38. Ghosh, A. K.; Hoek, E. M. V. Impacts of Support Membrane Structure and Chemistry on Polyamide–Polysulfone Interfacial Composite Membranes. *J. Membr. Sci.* **2009**, *336*, 140-148.
39. Kim, S. H.; Kwak, S.-Y.; Suzuki, T. Positron Annihilation Spectroscopic Evidence to Demonstrate the Flux-Enhancement Mechanism in Morphology-Controlled Thin-Film-Composite (TFC) Membrane. *Environ. Sci. Technol.* **2005**, *39*, 1764-1770.
40. Hermans, S.; Bernstein, R.; Volodin, A.; Vankelecom, I. F. J. Study of Synthesis Parameters and Active Layer Morphology of Interfacially Polymerized Polyamide–Polysulfone Membranes. *React. Funct. Polym.* **2015**, *86*, 199-208.
41. Tarboush, B. J. A.; Rana, D.; Matsuura, T.; Arafat, H. A.; Narbaitz, R. M. Preparation of Thin-Film-Composite Polyamide Membranes for Desalination Using Novel Hydrophilic Surface Modifying Macromolecules. *J. Membr. Sci.* **2008**, *325*, 166-175.
42. Khorshidi, B.; Thundat, T.; Fleck, B. A.; Sadrzadeh, M. A Novel Approach toward Fabrication of High Performance Thin Film Composite Polyamide Membranes. *Sci. Rep.* **2016**, *6*, 22069.
43. Khorshidi, B.; Thundat, T.; Fleck, B. A.; Sadrzadeh, M. Thin Film Composite Polyamide Membranes: Parametric Study on the Influence of Synthesis Conditions. *RSC Adv.* **2015**, *5*, 54985-54997.
44. Li, X.; Wang, K. Y.; Helmer, B.; Chung, T.-S. Thin-Film Composite Membranes and Formation Mechanism of Thin-Film Layers on Hydrophilic Cellulose Acetate Propionate Substrates for Forward Osmosis Processes. *Ind. Eng. Chem. Res.* **2012**, *51*, 10039-10050.
45. Bartmess, J. E.; Meot-Ner, M. M.; Lias, S. G.; Afeefy, H. Y.; Liebman, J. F.; Stein, S. E., Aniline. In *NIST Chemistry WebBook, SRD 69* [Online] National Institute of Standards and Technology: Gaithersburg, MD, 2017.
46. Zhang, X.; Cahill, D. G.; Coronell, O.; Mariñas, B. J. Absorption of Water in the Active Layer of Reverse Osmosis Membranes. *J. Membr. Sci.* **2009**, *331*, 143-151.
47. Matthews, T. D.; Yan, H.; Cahill, D. G.; Coronell, O.; Mariñas, B. J. Growth Dynamics of Interfacially Polymerized Polyamide Layers by Diffuse Reflectance Spectroscopy and Rutherford Backscattering Spectrometry. *J. Membr. Sci.* **2013**, *429*, 71-80.
48. Nakao, S.-i. Determination of Pore Size and Pore Size Distribution: 3. Filtration Membranes. *J. Membr. Sci.* **1994**, *96*, 131-165.
49. Chevalier, J. L. E.; Petrino, P. J.; Gaston-Bonhomme, Y. H. Viscosity and Density of Some Aliphatic, Cyclic, and Aromatic Hydrocarbons Binary Liquid Mixtures. *J. Chem. Eng. Data* **1990**, *35*, 206-212.
50. Behrisch, R.; Scherzer, B. M. U. Rutherford Back-Scattering as a Tool to Determine Electronic Stopping Powers in Solids. *Thin Solid Films* **1973**, *19*, 247-257.
51. Jeynes, C.; Barradas, N. P., Pitfalls in Ion Beam Analysis. In *Handbook of Modern Ion Beam Analysis*, Materials Research Society: Pittsburgh, 2010; Vol. 2.
52. Ammi, H.; Chekirine, M.; Allab, M. Slowing Down of Light Ions in Makrofol Kg Solid Nuclear Track Detector. *Radiat. Measur.* **2000**, *32*, 83-86.
53. Chekirine, M.; Ammi, H. Stopping Power of 1.0–3.0 Mev Helium in Mylar, Makrofol and Kapton Foils. *Radiat. Measur.* **1999**, *30*, 131-135.

54. Coronell, O.; Mariñas, B. J.; Cahill, D. G. Depth Heterogeneity of Fully Aromatic Polyamide Active Layers in Reverse Osmosis and Nanofiltration Membranes. *Environ. Sci. Technol.* **2011**, *45*, 4513-4520.
55. Khare, V. P.; Greenberg, A. R.; Krantz, W. B. Investigation of the Viscoelastic and Transport Properties of Interfacially Polymerized Barrier Layers Using Pendant Drop Mechanical Analysis. *J. Appl. Polym. Sci.* **2004**, *94*, 558-568.
56. Perry, L. A.; Coronell, O. Reliable, Bench-Top Measurements of Charge Density in the Active Layers of Thin-Film Composite and Nanocomposite Membranes Using Quartz Crystal Microbalance Technology. *J. Membr. Sci.* **2013**, *429*, 23-33.
57. Freger, V. Nanoscale Heterogeneity of Polyamide Membranes Formed by Interfacial Polymerization. *Langmuir* **2003**, *19*, 4791-4797.
58. Hohensee, G. T.; Hsieh, W.-P.; Losego, M. D.; Cahill, D. G. Interpreting Picosecond Acoustics in the Case of Low Interface Stiffness. *Rev. Sci. Instrum.* **2012**, *83*, 114902.
59. Khare, V. P.; Greenberg, A. R.; Krantz, W. B. Development of Pendant Drop Mechanical Analysis as a Technique for Determining the Stress–Relaxation and Water-Permeation Properties of Interfacially Polymerized Barrier Layers. *J. Appl. Polym. Sci.* **2003**, *90*, 2618-2628.
60. Greenberg, A. R.; Khare, V. P.; Krantz, W. B. Development of a Technique for the in-Situ Measurement of the Mechanical Properties of Ultra-Thin Interfacially Polymerized Films. *MRS Proceedings* **1994**, *356*, 541.
61. Losego, M. D.; Moh, L.; Arpin, K. A.; Cahill, D. G.; Braun, P. V. Interfacial Thermal Conductance in Spun-Cast Polymer Films and Polymer Brushes. *Appl. Phys. Lett.* **2010**, *97*, 011908.
62. Dong-Wook, O.; Seok, K.; A., R. J.; G., C. D.; Sanjiv, S. Interfacial Thermal Conductance of Transfer-Printed Metal Films. *Adv. Mater.* **2011**, *23*, 5028-5033.

TOC Figure

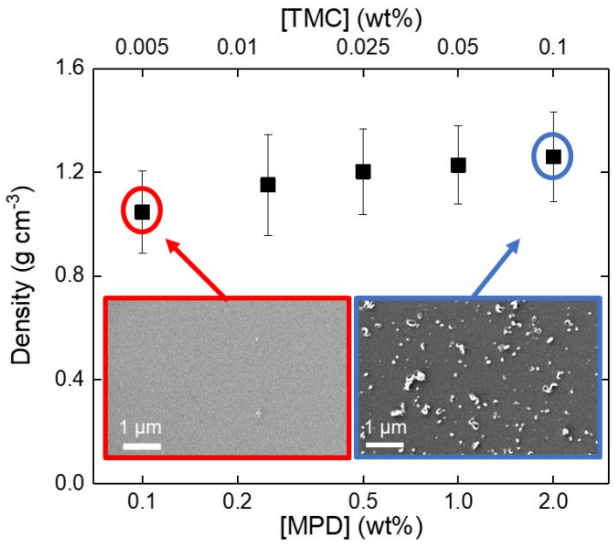
[TMC] (wt%)
0.005
0.01
0.025
0.05
0.1
Density (g cm^{-3})
1.6
1.2
0.8
0.4
0.0
1 μm
1 μm
0.1
0.2
0.5
1.0
2.0
[MPD] (wt%)